Simplified Models for Accelerated Structural Prediction of Conjugated Semiconducting Polymers

Michael M. Henry,[†] Matthew L. Jones,[†] Stefan D. Oosterhout,[‡] Wade A. Braunecker,[‡] Travis W. Kemper,[‡] Ross E. Larsen,[‡] Nikos Kopidakis,^{‡,§} Michael F. Toney,[¶] Dana C. Olson,[‡] and Eric Jankowski*,^{†,||}

†Micron School of Materials Science and Engineering, Boise State University, Boise ID 83725

‡National Renewable Energy Laboratory, Golden CO 80401 ¶SLAC National Accelerator Laboratory, Menlo Park CA 94025 §Department of Engineering, Macquarie University, Sydney NSW 2109, Australia ∥National Renewable Energy Laboratory, Golden CO 80401

E-mail: ericjankowski@boisestate.edu

Abstract

We perform molecular dynamics simulations of poly(benzodithiophene-thienopyrrolo-dione) (BDT-TPD) oligomers in order to evaluate the accuracy with which unoptimized molecular models can predict experimentally characterized morphologies. The predicted morphologies are characterized using simulated grazingincidence X-ray scattering (GIXS) and compared to the experimental scattering patterns. We find that approximating the aromatic rings in BDT-TPD with rigid bodies, rather than combinations of bond, angle, and dihedral constraints, results in 14% lower computational cost and provides nearly equivalent structural predictions compared to the flexible model case. The predicted glass transition temperature of BDT TPD $(410 \pm 32 \text{ K})$ is found to be in agreement with experiments. Predicted morphologies demonstrate short-range structural order due to stacking of the chain backbones (π - π stacking around 3.9 Å), and long-range spatial correlations due to the self-organization of backbone stacks into "ribbons" (lamellar ordering around 20.9 Å), representing the best-todate computational predictions of structure of complex conjugated oligomers. We find that expensive simulated annealing schedules are not needed to predict experimental structures here, with instantaneous quenches providing nearly equivalent predictions at a fraction of the computational cost of annealing. We therefore suggest utilizing rigid bodies and fast cooling schedules for high-throughput screening studies of semi-flexible polymers and oligomers to utilize their significant computational benefits where appropriate.

Introduction

Organic semiconducting polymers are promising components of next-generation electronics, as they can be used to create lightweight, flexible, and inexpensive devices such as organic thin film transistors (OTFTs), light emitting diodes (OLEDs), and photovoltaics (OPVs). These benefits arise from inexpensive, scalable, solution-based manufacturing processes, generally performed at lower temperatures than inorganic material purification, at atmospheric

pressure, and often without specialist machinery. ^{2,3} Additionally, synthetic chemists can functionalize components of these molecules, chemically tuning the energetics to obtain enhanced electronic performance. 4 Organic semiconductors are of particular interest in the photovoltaics community, where opportunities exist for scalable manufacturing of inexpensive solar technologies.⁵ Understanding how these molecules can be organized into structures that optimize conversion of light into electricity is a significant current challenge in the field.⁶ The nanostructure of OPV active layers is critically important to the charge-carrier mobility – a property that strongly affects the resulting device performance – and depends on thermodynamic and kinetic factors that govern the self-assembly of its constituent molecules. ^{7,8} In particular, the spacing between polymer backbones, the sizes of these ordered domains, and their interconnectivity – all morphological characteristics – have a significant impact on OPV performance. 9,10 In order to rationally design organic electronics, we require improved understanding of how to select components optimized to assemble into the desired nanostructures.

Current understanding of how OPV active layer morphologies depend on their components and processing has been developed through both wet lab experimentation and computer simulation. 11-15 In the laboratory, active layer films are made by mixing organic semiconductors with a compatible solvent that is later evaporated through spin coating, drop casting, printing, or other deposition techniques onto a substrate. 16,17 The nanostructure of these films can be probed using grazing-incidence Xray scattering (GIXS), which reveals ordering of the film components. 18 In computer simulations, molecular dynamics (MD) or Monte Carlo (MC) methods are used to sample equilibrium ensembles of configurations of the same molecules, and GIXS analysis can be extracted by transforming the atomic positions that result from these models. 15 The focus of this work is to enhance the complementarity of these techniques by improving the predictive capabilities of computer models.

The challenge in the lab is that determining

the relationships between active layer morphology and device performance is hindered by the difficulty in reliably controlling the morphology of organic thin films. One barrier in predicting the structures that self-assemble in organic semiconducting polymers is the impact small changes in materials choice or processing have on molecular packing. ¹⁹ For instance, the molecular weight ²⁰ and regionegularities ^{21,22} of poly(3-hexylthiophene) (P3HT) influences the conformation of backbone chains, structural feature sizes, and charge mobility of the deposited films. Furthermore, modifications to the casting solvent, ²³ annealing conditions, ^{21,24} or the addition of organic dyes ²⁵ can result in an active layer with drastically different structures and subsequent device performance. Another barrier to understanding active layer morphology is the difficulty of characterizing structure in relatively disordered layers with low scattering contrast. ¹⁸ Scanning microscopy techniques can provide useful insight into the surface features, but often miss the important structure of the bulk. Other techniques can provide additional information, but at the cost of destructively sampling the films. ²⁶

The challenge with molecular simulations lies in faithfully representing experiments with models that are computationally tractable. 15 Increasing the number of simulation elements either with more detail or larger systems increases the number of calculations to perform and therefore the computation time required to obtain the final result of the simulation. The time needed to perform a simulation -its computational cost- depends on: (1) the cost of advancing from one configuration to the next, which scales worse than linearly with the number of simulation elements (atoms), and (2) the fact that systems with more simulation elements require more configurations to be sampled before relaxing to a steady-state. In the case of organic semiconducting polymers, we can understand the scale of the problem by considering that coherence lengths of the order 3 to 30 nm are commonly observed in GIXS experiments. It stands to reason that, if a 30 nm coherence length is to be observed in a simulation, length scales of at least 30 nm must be represented. This is accomplished in MD simulations with a periodic unit cell, and filling it with carbons, hydrogens, oxygens, sulfurs, and nitrogens in representative ratios at realistic densities of the order 1 g/cm³, which corresponds to between 0.7 million and 1.5 million atoms. Million-atom simulations are now routine on supercomputers, especially those with graphics processing units (GPUs), but are typically limited to accessing time scales of hundreds of nanoseconds at most.²⁷ Performing a millionatom simulation of organic oligomers on supercomputers that accesses the hundreds or thousands of nanoseconds required to equilibrate can take several months of computation time for a single state point. In the polymer limit of chain length (over hundreds of monomers), neither experiments nor simulations can be run long enough to equilibrate, with observed morphologies representing entangled, kinetically arrested configurations. Rather than month-long computation times accessing equilibrium, the ability to perform hundreds of simulations per month that predict thermodynamically-driven yet possibly-arrested assembly, is required to determine phase diagrams or to find optimal conditions for assembling target structures.

To lower the computational cost of a model (assuming recent GPU supercomputers are being used), approximations must be invoked to lower the number of simulation elements represented. This is the basis behind coarsegraining strategies, where typically spherical simulation elements are used to represent collections of neighboring atoms and their associated bonds. Such models have been used to overcome the atomistic simulation time/length barrier, providing insight into photoactive polymers, lipid bilayers, and macromolecular structures. 13,14,28,29 Another modeling approximation is to ignore the fast modes of fluctuations about relatively rigid bonded constraints. Recent work studying the self-assembly of aromatic molecules perylene and perylothiophene showed that using rigid bodies to model conjugated systems improved sampling by a factor of two or better, without affecting the observed phase behavior or self-assembled morphology. ³⁰ The improvement was attributed to the combination of more timesteps accessible per CPU second, and shortened structural decorrelation times when a rigid body approximation was employed. Because conjugated systems are prevalent in organic electronics, coarse-grained models with rigid body approximations have potential to enable screening studies of organic electronic ingredients for those that robustly self-assemble into desirable nanostructures.

The success of computational screening studies depends on the accuracy and transferability of coarse-grained models. In this work we measure whether and to what degree rigid body approximations, combined with a united atom model, may be used to enhance the sampling efficiency of statepoints for a system that has characterized experimentally. We use MD simulations to investigate the self-assembly of poly(benzodithiophene-thienopyrrolodione) (BDT-TPD) pentamers, which are expected to be representative of donor-acceptor alternating copolymers. This class of molecules has demonstrated promise as a component of high power conversion efficiency photovoltaic devices, due to desirable optical and electrical properties. 31,32 We examine the evolution of the simulated morphologies after slow or fast cooling, and for cases when the conjugated moeities are described by rigid bodies or more expensive flexible bond, angle, and dihedral terms. Two different cooling schedules are used: an instantaneous "quench" from infinite temperature, and a more gradual "annealed" cooling schedule, where the temperature is decremented over a longer period of time. For all models, we evaluate the degree to which the simulations reproduce experimentally characterized film structures with simulated GIXS data, and quantify the computational efficiencies of each model. We aim to find the most efficient set of approximations to include in the modeling of an amorphous polymer that still faithfully predicts the morphologies observed in experiments. We determine that simulating BDT-TPD using rigid bodies results in a significant reduction to computational cost and reproduces experimentally-observed structure. We find that "annealing" results in structures that better match experiments than "quenching", as expected, but with minor measurable differences in precise scattering peak locations. We also observe small measurable differences between the predictions of rigid and flexible models, though both accurately predict primary experimental features, and the disorder-to-order (glass) transition temperature.

In the Methods section we define the rigid and flexible models used in this investigation as well as the analysis techniques used to quantify structure and determine when a simulation has sampled sufficiently many configurations. the Results section we detail the key simulation results and explain comparisons against experimental studies. We conclude with a discussion of the applicability of the present work and suggestions for future directions. The major modeling assumptions and investigation aims can be summarized in this question: To what degree do oligomers of BDT-TPD in implicit solvent and with implicit charges, modeled with OPLS-UA parameters unoptimized for BDT-TPD, faithfully represent self-assembly observed in experiments? We establish a minimum requirement for performing sufficiently accurate screening of thermodynamic state points, in order that promising structures can be quickly identified and submitted to further, more detailed, analvsis using more expensive and rigorous methods. The enhanced sampling of time scales and length scales presented here enables the best todate prediction of complex OPV oligomer selfassembly.

Methods

The chemical structure of BDT-TPD (Figure 1a) is described by a united atom model (Figure 1b), where hydrogen atoms are abstracted away into a "united" site that represents the carbon atom and all of its bonded hydrogens. ^{33,34} This technique reduces the number of simulation elements, improving computational efficiency while still maintaining good agreement with both atomistic models and experiment for a variety of systems. This technique has been shown to provide an improvement in computational efficiency, while still

maintaining good agreement with both atomistic models and experiment for a variety of systems. 30,35-39 We employ the OPLS-UA (Optimized Potential for Liquid Simulations-United Atom) forcefield to model the non-bonded and bonded interactions. ³³ The OPLS-UA forcefield includes constraints (bonds, angles, and dihedrals between pairs, triplets and quadruplets of simulation elements respectively) to model intramolecular structure, and describes nonbonded pair-wise interactions with Lennard-Jones potentials.³³ Reference units taken from the OPLS-UA force field are: length $\sigma = 3.55$ Å, energy $\varepsilon = 1.74 \times 10^{-21}$ J, and mass $\mathcal{M} =$ 32.06 amu. The values of σ and ε correspond to the van der Waals radius and Lennard-Jones well depth of OPLS sulfur atoms, and \mathcal{M} is the atomic mass of sulfur. The forcefield coefficients used in this investigation are described completely in the SI Section 1.

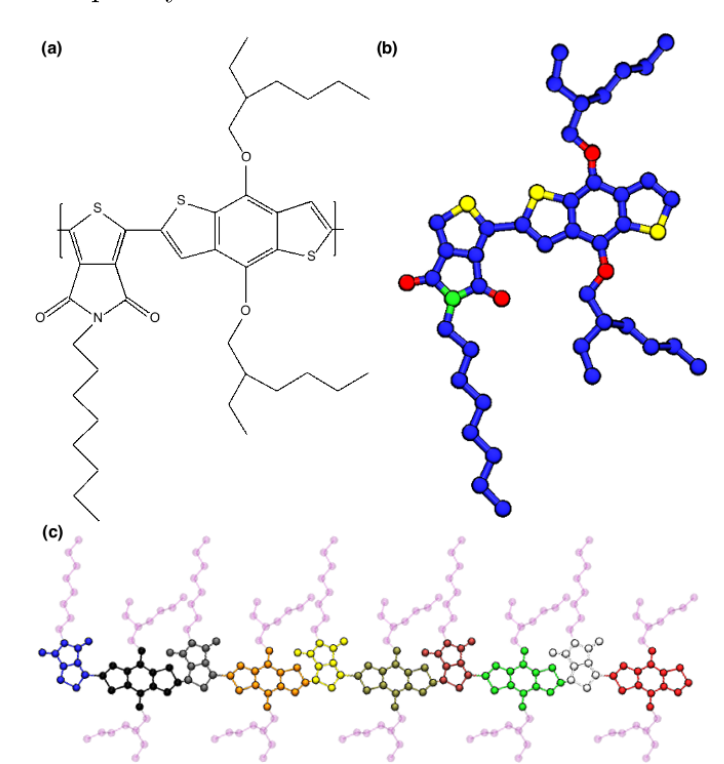


Figure 1: (a) Molecular structure of a BDT-TPD monomer. (b) United-atom topology of BDT-TPD, with implicitly modeled hydrogens. Blue spheres represent carbon atoms, red oxygen, yellow sulfur, and the green nitrogen. (c) An example BDT-TPD pentamer, colored by individual rigid bodies.

We consider two versions of the OPLS-UA

model of BDT-TPD. The first version, termed "flexible", is a standard implementation of the OPLS-UA force field as described above. The second version, termed "rigid", represents each of the benzodithiophene and thienopyrrolodione moieties as rigid bodies (Figure 1c).⁴⁰ Within each rigid body the constituent atoms are locked into place relative to each other, and a quaternion is used to encode the orientation of the individual benzodithiophene and thienopyrrolodione units. In both the rigid and flexible models, the oligomer sidechains are treated as flexible. Utilizing a rigid representation for these conjugated systems reduces the number of bond, angle, and dihedral degrees of freedom by 135, 200, and 290 respectively per pentamer, resulting in 53% fewer intramolecular constraints than in the flexible model. This reduction in the integrated degrees of freedom results in an increased quantity of simulated timesteps per CPU second. The current work focuses on whether this improved computational efficiency results in compromised sampling times or the structural prediction capabilities of the model.

We study oligomers with five repeat units of isotactic, regionegular BDT-TPD (Figure 1), each with molecular weight of 3.542 kDa in implicit solvent. These molecular weights permit the simulation of sufficient material to access experimentally relevant length scales, while avoiding the longer relaxation times associated with longer polymers. 13,14,41 The implicit solvent quality is determined by a multiplicative scaling parameter e_s that modulates the Lennard-Jones well depths as implemented by Shin et al. 42 Experimentally, $e_s < 1.0$ corresponds to a solvent within which a solute can be dissolved easily, and $e_s > 1.0$ describes a solvent that is more difficult to dissolve in. At the number densities studied here, the implicit solvent represents 18.2% of the simulation volume, and is meant to capture the mobility-enhancing effect of the solvent before it is evaporated from the active layer. This method allows us to capture the effects of a solvent, without the added computational cost of directly simulating the solvent molecules. In this investigation, we use $e_s = 0.5$ throughout to investigate the structure of BDT-TPD in a relatively good solvent. Here

we also assume long-range electrostatics play a negligible role in self-assembly, due to combined effects of charge screening by the implicit solvent and charge delocalization known to occur within conjugated systems. A performance benefit of the negligible charge assumption is that computationally expensive long-range electrostatic interactions need not be computed.

The reduced units of energy, distance, and mass determine derived units of time and temperature. The calculated units of time are therefore $\tau = \sqrt{\frac{M\sigma^2}{\varepsilon}} = 1.97 \times 10^{-12} \text{ s. A unit}$ of dimensionless temperature T corresponds to $\frac{\varepsilon}{k_B}$ = 126 K, and dimensionless temperatures between 0.5 T (63 K) and 9.0 T (1134 K) are used as thermostat setpoints in this work. We use the symbol T without units to refer to dimensionless temperature and specify units of Kelvin otherwise. Molecular dynamics simulations are performed using HOOMD-Blue^{40,43} on the Maverick and Kestrel high performance computing clusters outfitted with K20-architecture NVIDIA graphics processing units (GPUs). Simulations are performed in the canonical (constant number N, volume V, and temperature T) ensemble, regulated with the Nosé-Hoover thermostat 44 using the MTK equations. 45,46 Particle positions are updated via the velocity-Verlet integration of Newton's equations of motion, after every dimensionless timestep, dt = 0.001 = 1.97 fs. ⁴⁷ We perform simulations across a range of temperatures, T, and unless otherwise specified the fiducial simulation parameters are listed in Table 1.

Table 1: Fiducial simulation parameters: Periodic box length L, number of molecules N_{mol} , mixing temperature T_{mix} , solvent quality e_s , and timestep size dt.

L	30.017σ	10.7 nm
$T_{\rm mix}$	9.5	1198 K
dt	0.001	$1.97 \times 10^{-15} \text{ s}$
$N_{\rm mol}$	197	197
e_s	0.5	good solvent

Initial configurations are generated through random chain placement, mixing, and shrinking to the target density described below. X-Ray reflectivity measurements of poly(BDT-TPD) report 1.17 g/cm³, 48 and here we initialize volumes of BDT-TPD oligomers with a small amount (18.2% by volume) of implicit solvent. First, the 197 pentamers are randomly initialized in volume large enough to easily place them without overlap. Second, NVT simulations are run at $T_{\text{mix}} = 9.5 \text{ (1198 K) for } 1.0 \times 10^5$ timesteps (0.197 ns), allowing the pentamers to mix at high temperature and low density. Finally, an additional 1×10^5 timesteps (0.197) ns) of this simulation are performed while the periodic box axes are linearly scaled down to 30.017σ . This initialization protocol efficiently generates unique, randomized configurations of oligomers at T = 9.5 (1198 K) that are then annealed or quenched to lower temperatures. When cooled below the glass transition temperature, the oligomers phase separate from the implicit solvent so we expect the resulting structures to be comparable to neat BDT-TPD films after solvent evaporation.

The "annealed" simulations model gradual cooling of BDT-TPD films. Annealing is modeled here with a sequence of MD simulations performed at successively lower temperatures. The dimensionless temperatures in these simulations are decremented instantaneously by $\delta T = 0.5$ (63 K), every 1.2 $\times 10^7$ timesteps $(\sim 24 \text{ ns})$ resulting in a cooling rate of 2.62 Kelvin per nanosecond. Though this annealing rate is extremely fast compared to those achievable in experiments, for the relatively small volumes simulated here it makes the difference between allowing volumes to relax towards thermodynamic equilibrium versus ensuring kinetic arrest. Nineteen simulations are performed for each annealing run, beginning at T = 9.5 (1198 K) and ending at T = 0.5 (63)K). The "quenched" simulations model cooling schedules that kinetically arrest the structure of BDT-TPD films before they are able to sample the thermodynamically stable configurations that drive self-assembly. Polymer films that have been drop-cast or spin-coated in experiments are assumed to be quenched, as subsequent annealing results in significant ordering^{20,49–52} Here, we implement quenched cooling schedules by instantaneously changing the temperature of an initial $T=9.5~(1198~{\rm K})$ configuration to the desired set point. We quench to the same nineteen temperatures as sampled during the annealing schedule. This permits the differences in structure between cooling schedules to be observed at each of the 19 state points.

Quenched simulations can be performed in parallel if multiple processors or GPUs are available, whereas annealed simulations must be performed in series. Therefore, if all other factors are equal, it is computationally advantageous to be able to perform quenched simulations. All other factors are usually not equal when comparing equilibrated to non-equilibrium structures (initial conditions matter, integrators can matter, etc), so we expect the utility of quenching models to be limited to the specific case of modeling polymer films that are kinetically arrested.

Simulations are determined to be in thermodynamic equilibrium by comparing the fluctuations in potential energy of a simulation, run for at least twenty times the expected relaxation time from preliminary investigations. First, the evolution of the Lennard-Jones pair potential energy, E_{LJ} , is considered for each simulation, and split into 10 bins. For each bin, the standard deviation in E_{LJ} is calculated. Starting from the final bin and working backwards through simulation time, bins are added to the "equilibrated region" if the standard deviation of the bin's potential energy is no more than twice that of the previous bin in the region.

Once the equilibrated region is determined, its autocorrelation time is calculated to obtain the number of timesteps between statistically independent trajectory frames. An example is shown in figure Figure 2, where data after 1×10^{-7} s are considered to be within the equilibrated window. The autocorrelation time measured by the first zero of the self-correlations of the equilibrated windows (SI Section 2) averages 1.08×10^6 timesteps (2.12 ns) for the four combinations of model flexibility and cooling schedule. The slowest autocorrelation time measured was 2.11×10^7 timesteps (41.6 ns). Simulation configurations are saved every 1×10^6 timesteps in accordance with the

average autocorrelation times.

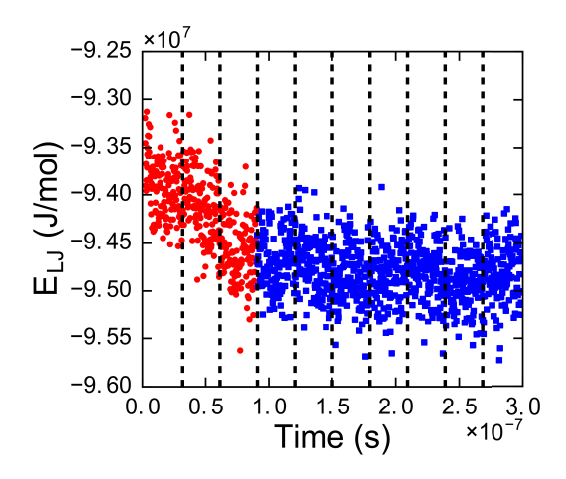


Figure 2: A representative non-bonded potential energy trajectory E_{LJ} . These data correspond to the flexible annealed simulation at $T=2.0~(252~\mathrm{K})$. The blue squares describe the equilibrated region of the system, where the standard deviation of energies within each bin (represented by the vertical, black dashes) is no more than twice that of the region to the right of it. Red circles describe the region of the simulation trajectory where the potential energy has not yet relaxed to equilibrium. The Python plotting library Matplotlib is used to generate the plots within this work.⁵³

Determining structure

The morphological structure of each cooled system is examined through a combination of cluster analysis and simulated X-ray diffraction. Here, neighboring oligomers are considered to be part of the same cluster if the centers-ofmass of at least two adjacent monomers on each chain are located within 1.6σ of each other. Ensuring that TPD moieties on each chain are within the defined center-of-mass cutoff suggests that there will be sufficient molecular orbital overlap between the regions of the molecule that a charge carrier is likely to be delocalized along, resulting in favorable charge transport. Defining clusters in this manner has the effect of identifying the aggregates within the morphology that would be expected to have good inter-chain electronic charge transport -

an important characteristic for efficient photovoltaic devices. 54,55 Figure 3 shows an example of two clusters. The chains within each cluster satisfy the clustering criterion, however the criterion is not satisfied between the two clusters because only a single monomer of each change lies within the 1.6σ cut-off. Distinguishing clusters of BDT-TPD by color gives a visual representation of structure, in which significant ordering is apparent as BDT-TPD is cooled, as seen in the Visual Molecular Dynamics visualizations (Figure 4). 56,57

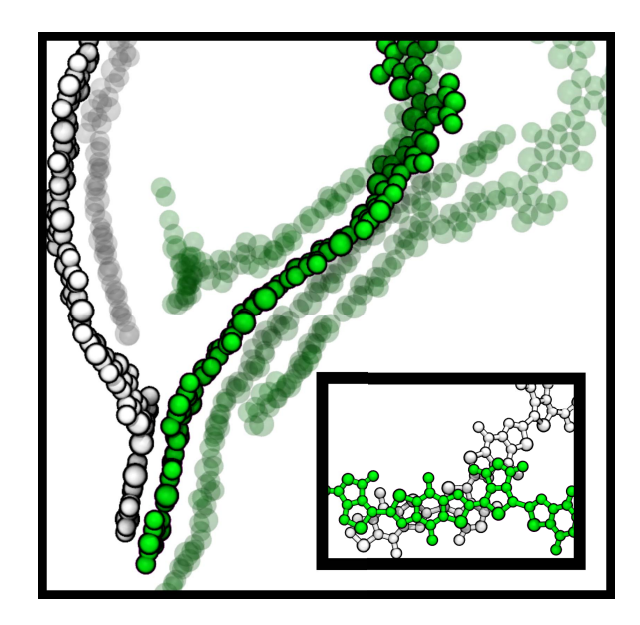


Figure 3: An example of two independent clusters (green and white) that do not satisfy our clustering criterion, due to an insufficient number of adjacent backbone moeities within the center-of-mass cut-off for the most external molecules. Only a single green monomer is within 1.6σ of a white monomer (see insert).

Quantification of the coherence length scales in each simulation snapshot is performed by a simulated grazing incidence X-Ray scattering technique. The full details of the simulation methodology, including the mathematical implementations of sample orientation and structure factor calculation, can be found in Ref. 15. In order to automate the extraction of any coherence length scales and to quantify the degree to which they appear in a simulation snapshot, we perform ensemble averages of scattering features over spherically-distributed orientations of the simulation snapshot. These coherence

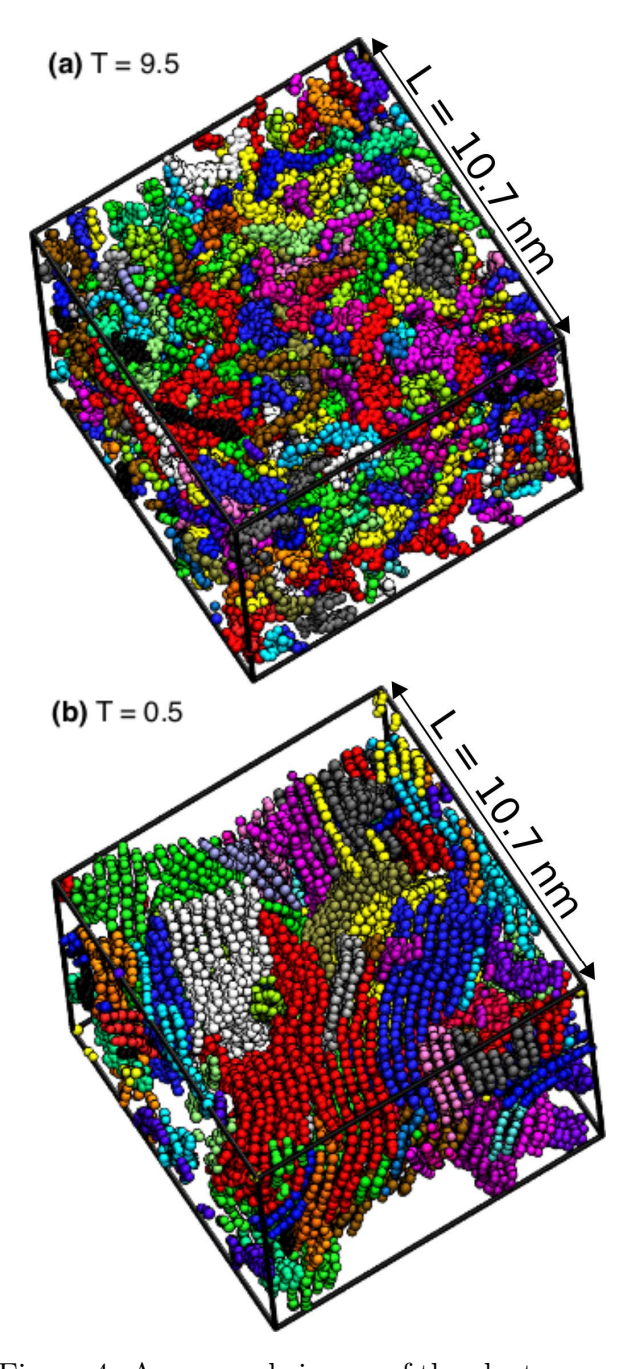


Figure 4: An example image of the clusters generated using our specified criteria within the flexible BDT-TPD morphology, taken at (a) the $T=1198~\rm K$, and (b) after gradual annealing down to $T=63~\rm K$. For clarity, only the chain backbone moieties are depicted, and like colorings indicate simulation elements that belong to the same cluster. Cluster domains are a few nanometres in size and the simulation volume is cubic.

length scales represent averages over 100 orientations of the simulation volume, uniformly distributed about a sphere using the generalized

spiral approximation.⁵⁸ Each individual scattering pattern captures any anisotropic structural features associated with its scattering orientation and the spherical averaging facilitates the extraction of the most significant structural periodicities. The chain packing is described by the arrangement of the polymer backbone moieties within the sample. As our simulations contain fewer, shorter chains and smaller simulation volumes than are available in experiment, we remove the aliphatic side-chains in order to amplify the signal associated with this backbone structure. To facilitate automated feature detection from the 2D GIXS patterns, we compute structure factors from the radial (q_r) average of diffraction intensities. An example of the structure factor plot at T = 315 K for all four models can be seen in Figure 5. The location and amplitude of the various peaks in Figure 5 are dependent on the combination of the pair interaction potentials, the choice of e_s , the final temperature of the simulation, and whether it was quenched or annealed.

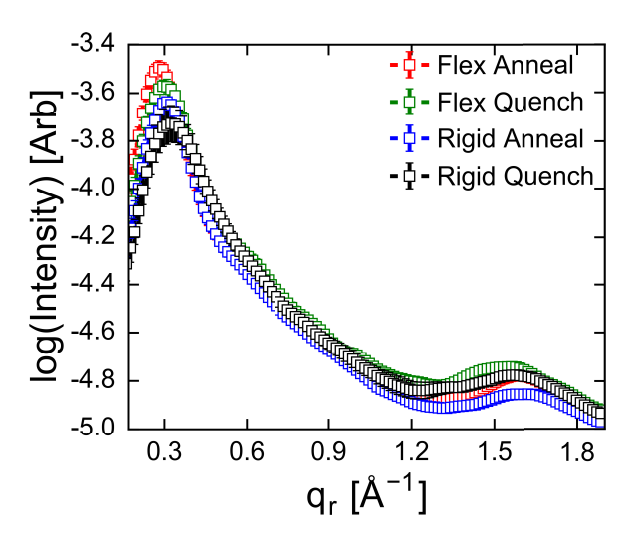


Figure 5: The logarithm of the intensity in the scattering pattern as a function of radially-averaged structure factors (q_r) for each model at T = 315 K.

We compare the calculated diffraction pattern with experimental GIXS data to validate our models. This practice is particularly useful when there is a match between experimental and simulated scattering patterns, because it gives insight into possible atomistic arrangements that occur in the experimental systems. Matching scattering patterns do not guarantee that the simulated structures are present in experimental films, ⁵⁹ yet represent the most detailed insight into possible structures without developing more sophisticated experimental characterization methods.

Results

MD simulations of the "rigid" and "flexible" models of BDT-TPD oligomers are equilibrated using the "annealed" and "quenched" cooling schedules at nineteen temperatures for each of the four combinations of model and cooling schedule (flexible-annealed, flexible-quenched, rigid-annealed, and rigid-quenched cases). Ensemble average properties are calculated from statistically independent configurations once the simulation has relaxed as described in the Methods section. On average it took 5×10^6 timesteps (9.85 ns) to reach a steady-state after which the average potential energy autocorrelation times for each state point were 1.08×10^6 timesteps (2.12 ns). We evaluate the computational performance of each model and cooling schedule combination. Additionally, we compute three ensemble properties to characterize each trajectory, (1) the non-bonded potential energy E_{LJ} , (2) the proportion of chains belonging to a cluster ζ , and (3) simulated scattering patterns.

Performance

The computational performance of the four cases are compared by evaluating timesteps per second (TPS), relaxation time, and autocorrelation time at each temperature. Figure 6 shows the rigid model has roughly 14% higher TPS compared to the flexible model at the same temperature, and that there is little difference in TPS between quenching and annealing schedules, as expected. Prior work employing rigid models for perylene and perylothiophene showed the rigid model could have significantly different relaxation times and autocorrelation times.³⁰ Here we find the flexible and rigid models have identical autocorrelation

and relaxation times, which means that TPS is an accurate metric for comparing computational efficiency. A more thorough and complete discussion of our simulations' relaxation and autocorrelation times is included in SI Section 2.

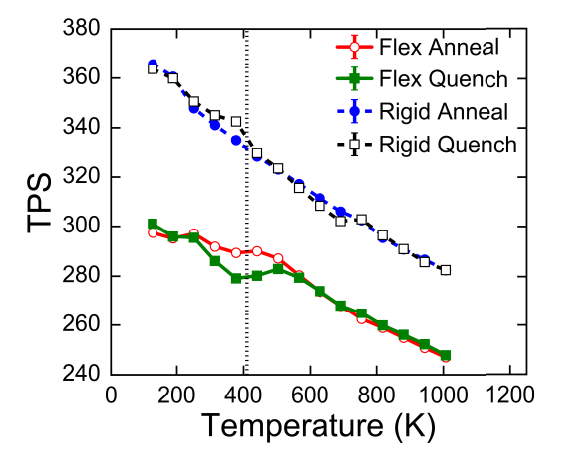


Figure 6: The TPS of the simulations explored in this investigation as a function of temperature. The black vertical line indicates the disorder-order transition temperature $T_{\rm DO}=410~{\rm K}.$

Potential Energy

Using E_{LJ} as a proxy for structure we find the annealed and quenched simulations generate identical potential energies when $T \geq 504 \text{ K}$ (Figure 7a). For cooler temperatures (T < 504K) we find the annealed runs achieve lower potential energies than their quenched counterparts, as expected. In each case, E_{LJ} is averaged over statistically independent samples. In all four cases, we observe a change in slope of the potential energy below 504 K, which is consistent with a structural phase transition. We observe the largest structural changes to occur between 441 K and 378 K, so we use the average as the disorder-order transition temperature $T_{\rm DO} = 410$ K. This corresponds well with the glass transition temperature (411 K) measured in experiments, 60 although we note the presence of significant (8%) uncertainties both here and in experiments. The non-bonded potential energies are more positive in the rigid case

because pairwise interactions between components of a rigid body (which would typically be negative) are omitted. The differences in non-bonded potential energy between the rigid and flexible cases are not constant, which suggests that these models may give rise to different molecular arrangements. (Figure 7b). However, since differences in E_{LJ} are merely a proxy for structure, a more direct measurement of structure is warranted.

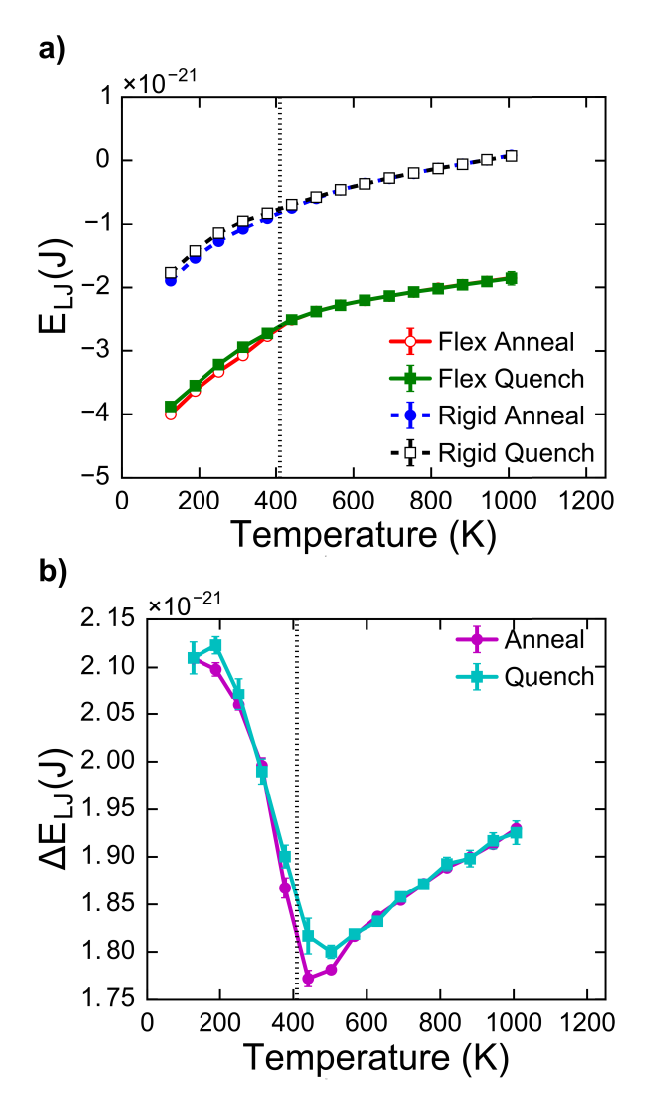


Figure 7: a) Non-bonded potential energy E_{LJ} per atom as a function of temperature, T. b) Energy difference per atom between the rigid and flexible models. Error bars indicate standard error. Black vertical lines indicate the locations of the disorder-order transition temperature $T_{\rm DO}=410~{\rm K}.$

Clustering

To provide more detailed structural information about morphologies around the transition temperature $T_{\rm DO}$, we analyze and visualize clusters of oligomer backbones as described in the Methods section. Figure 4 shows flexible-annealed morphologies above and below T_{DO} , with backbones colored according to the cluster that they belong to. The ordering of backbones within clusters can be seen in Figure 4b. Details of a single cluster are shown in Figure 8, where two orientations of the cluster describe the stacks of backbones that form "ribbons". This backbone aggregation corresponds to π -stacking observed experimentally, and we observe an average separation of around 4 Å. Such stacking is beneficial for charge transport, as closely stacked chains lead to increased orbital overlap and faster inter-molecular carrier hops, which can be critical in obtaining the high device efficiencies in organic thin-films. 54,55 We find that the average spacing between ribbons, similar to the lamellar length scale observed experimentally, is around 21 Å for all four model/cooling combinations.

Analyzing the proportion of clustered backbones, ζ , as a function of temperature for the four cases (Figure 9) gives additional insight into their structural differences. As expected, both the quenching and annealing models give the same ζ when $T > T_{DO}$. However, the rigid models are more likely to have clustered chains when $T > T_{DO}$ than the flexible models. Near $T_{\rm DO}$, all four cases demonstrated sharp increases in ζ . For low temperatures $T < T_{DO}$, the quenched cases demonstrated a relative decrease in ζ , which is consistent with the prior results indicating that they lack the thermal energy to rearrange into thermodynamically stable configurations. The annealed cases both show increased clustering as temperature is lowered, though the flexible-annealed case ordered more than the rigid-annealed case. These results reinforce the observations that a structural transition occurs around 410 K and that modeling conjugated systems with rigid bodies has a measurable impact on the π - π structural features that emerge.

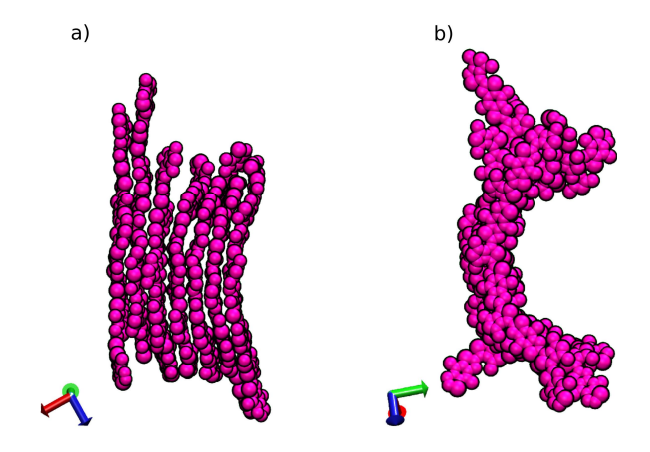


Figure 8: A detailed view of a single cluster, viewed from two orientations, taken from a $T=315~\rm K$ flexible-annealed simulation snapshot. The red, green, and blue arrows represent the x, y, and z axis respectively. a) When the cluster is viewed along the y-axis, the aggregation of backbones through pi-stacking can be observed. b) When the cluster is viewed along the x-axis, the stack of backbones are seen to be mostly in-register. We refer to these clusters as "ribbons".

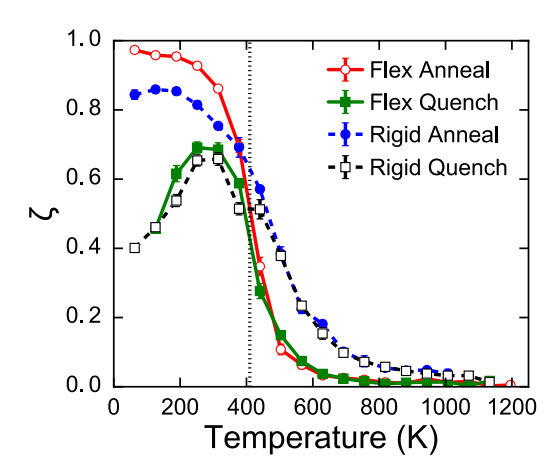


Figure 9: The proportion of chains that belong to a cluster containing two or more molecules (ζ) , averaged over all statistically independent frames for each state point, cooling schedule and molecular model investigated. The black vertical line indicates the disorder-order transition temperature $T_{\rm DO}=410~{\rm K}.$

Scattering

For each of the four combinations of flexibility and cooling schedule, we find simulated diffrac-

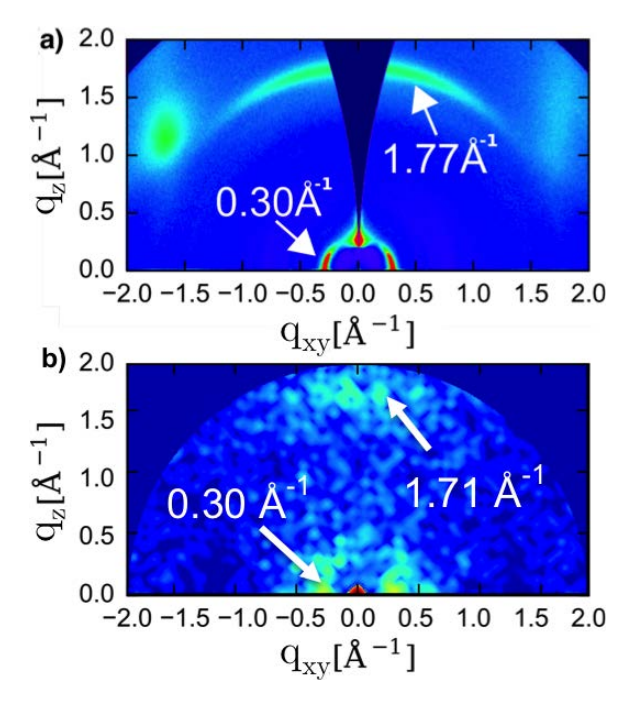


Figure 10: Comparison of a single a) experimental, and b) simulated GIXS scattering pattern of a BDT-TPD morphology. The simulated system contains oligomers described by rigid bodies, that were annealed to a temperature of 315 K, and the snapshot was taken from the sample orientation that most clearly showed perpendicular features.

tion patterns that closely match experimental scattering patterns. Below the disorderorder transition temperature $T_{DO} = 410 \text{ K}$, GIXS patterns for all four combinations have the same twofold rotational symmetry with orthogonal scattering peaks around 0.30 Å^{-1} and 1.77 Å^{-1} . Figure 10a presents the experimental X-ray scattering data obtained for BDT-TPD (synthesis described in SI Section 3 and Ref 61), in which prominent peaks are observed at $q_r = 0.30 \text{ Å}^{-1} (r_{\text{lamellar}} = 20.9 \text{ Å})$ and 1.77 Å⁻¹ $(r_{\pi-\pi} = 3.5 \text{ Å})$. Figure 10b presents a representative simulated scattering pattern taken from a T = 2.5 (315 K) rigid annealed simulation. The simulated diffraction peaks are measured at 0.30 Å⁻¹ and 1.71 Å⁻¹, echoing the length scales observed during our clustering analysis, and in excellent agreement with experiment.

We compare the average peak locations at T = 2.5 (315 K), where all four combinations of model and cooling schedule demonstrate sig-

nificant clustering. Averaging over all independent frames and all scattering orientations at T = 315 K showed that the rigid annealed system most closely matched the experimental scattering patterns, with only a 3.34% error in lamellar spacing, and a 10.57\% error in π - π spacing. However, the π -stacking lengths across all four models lie within 15.71% (0.55 Å), and lamellar spacing within 6.70% (1.4 Å) of the experimental values, suggesting only minor structural differences between the models. In all four model and cooling schedule combinations, the π -stacking length scales (3.87 < $r_{\pi-\pi}$ < 4.05 Å) are predicted to be larger than those observed in experiments $(r_{\pi-\pi}=3.5 \text{ Å})$, as seen in ta-This corresponds to a 12.41% overestimation of the physical π -stacking distance on average, which would be expected due the equilibrium distance between OPLS-UA sulfurs: The minimum of the Lennard-Jones potential is at $2^{1/6}\sigma$, or 1.12σ , which for sulfur is 3.98 Å. The OPLS-UA forcefield was not optimized for conjugated systems, and this observation suggests that new atom types with smaller diameters to represent conjugated carbons and sulfurs may be a small addition to OPLS-UA that will offer improved structural predictions for conjugated molecules. The periodicity of the long-ranged lamellar length scales (around $r_{\text{lamellar}} = 20.9 \text{ Å}$) is in better experimental agreement, as all four of our models predict length scales $19.5 < r_{\text{lamellar}} < 22.2 \text{ Å}$, within 6.70% of experimental GIXS data. The OPLS-UA forcefield is well parameterized for alkyl sidechains, which are expected to mediate the long length scales in our system, accounting for the good agreement with experiment.

Table 2: Comparison of the lamellar (r_{lamellar}) and π -stacking $(r_{\pi-\pi})$ structural features and their deviation from the experimental values $(r_{\text{expt, }\pi-\pi}=3.5 \text{ Å}, r_{\text{expt, lamellar}}=20.9 \text{ Å})$ at T=2.5. The subscript 'sim' corresponds to simulated peak locations.

	Long-range $(r_{lamellar})$			Short-range $(r_{\pi-\pi})$		
	$r_{ m sim}$	$r_{\rm sim} - r_{\rm expt}$	$ r_{\text{sim}} - r_{\text{expt}} \%$	$r_{ m sim}$	$r_{\rm sim} - r_{\rm expt}$	$ r_{\text{sim}}-r_{\text{expt}} $ 07
Model	(Å)	(Å)	r _{expt} /0	(Å)	(Å)	r _{expt} /0
Flex Anneal	22.25 ± 0.06	+1.35	6.46	3.937 ± 0.008	+0.437	12.49
Flex Quench	20.9 ± 0.4	+0.0	0.00	4.05 ± 0.03	+0.55	15.71
Rigid Anneal	20.2 ± 0.2	-0.7	3.34	3.87 ± 0.04	+0.37	10.57
Rigid Quench	19.5 ± 0.2	-1.4	6.70	3.88 ± 0.04	+0.38	10.86

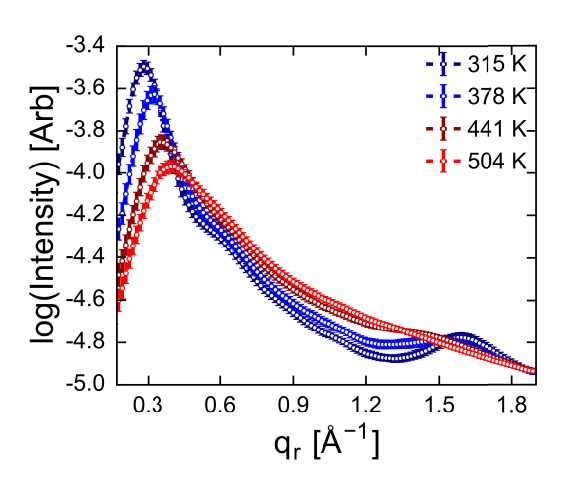


Figure 11: The logarithm of the scattering intensity as a function of radially-averaged structure factors (q_r) over each statistically independent frame for a representative flexible-annealed system at simulation temperatures above and below $T_{\rm DO}=410K$. Only one model is shown for clarity as all four combinations of cooling schedules and models demonstrated the same trend.

Emergence of increased ordering via simulated scattering analysis supports the observations from our non-bonded potential energy measurements and clustering data that T_{DO} = 410K. In Figure 11, we consider the scattering peak intensities averaged over statistically independent frames at four temperatures for representative rigid-quenched simulations. As the temperature is lowered, the intensity of the low $q_r \sim 0.3 \text{ Å}^{-1}$ peak increases and shifts downwards, corresponding to longer length scales. This indicates that there is more and longerrange structural ordering present in the morphology at lower temperatures, in analogy to lamellar and liquid crystal formation observed in neat poly(3-hexylthiophene)-b-poly-(90,90dioctylfluorene) (P3HT-b-PF) thin films. 62 At high $q_r \sim 1.6 \text{ Å}^{-1}$, there is a local peak intensity maximum corresponding to increased π stacking order in the system when cooled below $T_{\rm DO}$, but this feature is not observed when $T > T_{\rm DO}$. The presence of the π -stacking peak at T < 410 K reinforces that a structural change is occurring in the system when cooling from above $T_{\rm DO}$ to below it.

Conclusions

The OPLS-UA model used in this investigation captures the phase behavior of BDT-TPD, with both rigid and flexible models showing a glass transition temperature around 410 ± 32 K, in agreement with the glass transition temperature (411 K) measured in experiments.⁶⁰ Utilizing rigid bodies to model conjugated systems in BDT-TPD results in 14% faster simulations that faithfully reproduce the structural characteristics observed in experiments. Cooling BDT-TPD oligomers below 441 K gives rise to increasingly ordered stacks of polymer backbones ("ribbons"), with π -stacking within the ribbons and the "lamellar" spacing between the ribbons for both rigid and flexible models, whether they are annealed or quenched. All four combinations of model and cooling schedule overpredict the π -stacking length (by 0.37) Å to 0.55 Å), which is not surprising considering the OPLS-UA forcefield is not optimized for these conjugated backbones. All of the model and cooling combinations predict the lamellar spacing within 1.35 Å of the experimental value, with the flexible-quench matching best. Overall, the rigid-annealed simulations best match experiments with the closest prediction of π stacking and only 3.34% error in lamellar spacing, and the rigid-quenched simulations provide the most structural insight for the least computation. In short, we find the phase behavior and morphology of BDT-TPD to be accurately predicted by GPU-accelerated simulations of short oligomers in implicit solvent using the OPLS-UA force-field without explicit long-range electrostatics.

The accurate structural predictions observed here support the modeling assumptions that the partial charges of BDT-TPD, the solvent degrees of freedom, and the flexibility of each conjugated monomer unit play negligible roles in determining self-assembled structure. We interpret these results to indicate that these modeling assumptions are justified for accelerating the prediction of organic photovoltaic morphologies. This is an important result in the context of high-throughput simulations needed to screen thousands of candidate chemicals for

those most likely to result in high-efficiency organic photovoltaics because it shows that "offthe-shelf" force fields that have not been optimized for a particular chemistry have high predictive utility. The computational efficiency of quenching compared to annealing is significant, as here a single 12-hour quench gives as experimentally-relevant results as over 144 hours of annealing. We recommended using computationally efficient techniques (rigid bodies, instantaneous quenching) for estimating phase transitions and identifying candidate phases, followed by more detailed explorations where appropriate. As one example relevant to organic photovoltaics, we show in other work how back-mapping atomistic detail for calculating properties such as charge mobility is essential. ¹⁵ Of course, there are certainly moeties for which charge, flexibility, and solvent assumptions made here will break down, so chemical intuition or first-principles calculations should be used before blindly applying them.

Using a simplified united atom model to predict BTD-TPD oligomer structure opens related questions that extend from this work. Firstly, to what degree can BDT-TPD and related organic semiconductors be further coarsegrained before the increases in sampling efficiency are outweighed by inaccuracies in structural predictions? Secondly, are there fundamental limits to using coarse-graining and backmapping as a form of thermodynamic integration to more rigorously calculate free energy differences between materials? Thirdly, how generally applicable is the rigid-body assumption for conjugated systems? Answering these questions and further validating our modeling assumptions by predicting the morphologies of as vet unsynthesized organic semiconductors is the focus of future work.

Acknowledgements

This work used the Extreme Science and Engineering Discovery Environment (XSEDE), which is supported by National Science Foundation grant number ACI-1053575.⁶³ This material is based upon work supported by the Na-

tional Science Foundation under Grants No. (1653954) and (1229709). Use of the Stanford Synchrotron Radiation Lightsource, SLAC National Accelerator Laboratory, is supported by the U.S. Department of Energy, Office of Science, Office of Basic Energy Sciences under Contract No. DE-AC02-76SF00515. TWK, REL, NK and DCO acknowledge support from the Organic Photovoltaic SuNLaMP program, which is funded by the U.S. Department of Energy under Contract No. DE-AC36-08-GO28308 with the National Renewable Energy Laboratory through the DOE Solar Energy Technologies Program. MMH was supported by a NASA Idaho Space Grant Consortium fellowship, which is funded by NASA (NNX15Ai04H). We thank Alex Ayzner for his useful conversations.

Supporting Information

Simulation code repositories; determining equilibrium; BDT-TPD synthesis; computational hardware used in this study.

References

- (1) Heeger, A. J. Semiconducting Polymers: The Third Generation. *Chemical Society Reviews* **2010**, *39*, 2354.
- (2) Arias, A. C.; MacKenzie, J. D.; McCulloch, I.; Rivnay, J.; Salleo, A. Materials and Applications for Large Area Electronics: Solution-based Approaches. *Chemical Reviews* **2010**, *110*, 3–24.
- (3) Krebs, F. C.; Tromholt, T.; Jørgensen, M. Upscaling of Polymer Solar Cell Fabrication Using Full Roll-to-roll Processing. *Nanoscale* **2010**, *2*, 873.
- (4) Li, Y. Molecular Design of Photovoltaic Materials for Polymer Solar Cells: Toward Suitable Electronic Energy Levels and Broad Absorption. *Accounts of Chemical Research* **2012**, *45*, 723–733.

- (5) Espinosa, N.; Hösel, M.; Angmo, D.; Krebs, F. C. Solar Cells with One-day Energy Payback for the Factories of the Future. *Energy & Environmental Science* **2012**, *5*, 5117.
- (6) Anthony, J. E. Organic Electronics: Addressing Challenges. *Nature Materials* **2014**, *13*, 773–775.
- (7) Sirringhaus, H. 25th Anniversary Article: Organic Field-effect Transistors: The Path beyond Amorphous Silicon. Advanced Materials **2014**, 26, 1319–1335.
- (8) Jones, M. L.; Huang, D. M.; Chakrabarti, B.; Groves, C. Relating Molecular Morphology to Charge Mobility in Semicrystalline Conjugated Polymers. *Journal of Physical Chemistry C* **2016**, *120*, 4240–4250.
- (9) Bartelt, J. A.; Beiley, Z. M.; Hoke, E. T.; Mateker, W. R.; Douglas, J. D.; Collins, B. A.; Tumbleston, J. R.; Graham, K. R.; Amassian, A.; Ade, H. et al. The Importance of Fullerene Percolation in the Mixed Regions of Polymer-Fullerene Bulk Heterojunction Solar Cells. Advanced Energy Materials 2013, 3, 364–374.
- (10) Noriega, R.; Rivnay, J.; Vandewal, K.; Koch, F. P. V.; Stingelin, N.; Smith, P.; Toney, M. F.; Salleo, A. A General Relationship Between Disorder, Aggregation and Charge Transport in Conjugated Polymers. Nat Mater 2013, 12, 1038– 1044.
- (11) Brabec, C. J.; Gowrisanker, S.; Halls, J. J. M.; Laird, D.; Jia, S.; Williams, S. P. Polymer-fullerene Bulk-heterojunction Solar Cells. Advanced Materials 2010, 22, 3839–3856.
- (12) Dou, L.; You, J.; Hong, Z.; Xu, Z.; Li, G.; Street, R. a.; Yang, Y. 25th Anniversary Article: A Decade of Organic/Polymeric Photovoltaic Research. Advanced Materials 2013, 25, 6642–6671.

- (13) Jankowski, E.; Marsh, H. S.; Jayaraman, A. Computationally Linking Molecular Features of Conjugated Polymers and Fullerene Derivatives to Bulk Heterojunction Morphology. *Macromolecules* 2013, 46, 5775–5785.
- (14) Marsh, H. S.; Jankowski, E.; Jayaraman, A. Controlling the Morphology of Model Conjugated Thiophene Oligomers through Alkyl Side Chain Length, Placement, and Interactions. *Macromolecules* **2014**, *47*, 2736–2747.
- (15) Jones, M. L.; Jankowski, E. Computationally Connecting Organic Photovoltaic Performance to Atomistic Arrangements and Bulk Morphology. *Molecular Simulation* **2017**, *43*, 756–773.
- (16) Krebs, F. C. Fabrication and Processing of Polymer Solar Cells: A Review of Printing and Coating Techniques. Solar Energy Materials and Solar Cells 2009, 93, 394– 412.
- (17) Vongsaysy, U.; Bassani, D. M.; Servant, L.; Pavageau, B.; Wantz, G.; Aziz, H. Formulation Strategies for Optimizing the Morphology of Polymeric Bulk Heterojunction Organic Solar Cells: A Brief Review. *Journal of Photonics for Energy* **2014**, *4*, 040998.
- (18) DeLongchamp, D. M.; Kline, R. J.; Herzing, A. Nanoscale Structure Measurements for Polymer-fullerene Photovoltaics. *Energy & Environmental Science* **2012**, *5*, 5980–5993.
- (19) Peet, J.; Senatore, M. L.; Heeger, A. J.; Bazan, G. C. The Role of Processing in the Fabrication and Optimization of Plastic Solar Cells. *Advanced Materials* **2009**, *21*, 1521–1527.
- (20) Zen, A.; Pflaum, J.; Hirschmann, S.; Zhuang, W.; Jaiser, F.; Asawapirom, U.; Rabe, J. P.; Scherf, U.; Neher, D. Effect of Molecular Weight and Annealing

- of Poly(3-hexylthiophene)s on the Performance of Organic Field-effect Transistors. *Advanced Functional Materials* **2004**, *14*, 757–764.
- (21) Surin, M.; Leclere, P.; Lazzaroni, R.; Yuen, J. D.; Wang, G.; Moses, D.; Heeger, A. J.; Cho, S.; Lee, K. Relationship between the Microscopic Morphology and the Charge Transport Properties in Poly(3-hexylthiophene) Field-effect Transistors. *Journal of Applied Physics* **2006**, 100, 033712.
- (22) Kim, Y.; Cook, S.; Tuladhar, S. M.; Choulis, S. A.; Nelson, J.; Durrant, J. R.; Bradley, D. D. C.; Giles, M.; McCulloch, I.; Ha, C.-S. et al. A Strong Regioregularity Effect in Self-organizing Conjugated Polymer Films and High-efficiency Polythiophene:fullerene Solar Cells. Nature Materials 2006, 5, 197–203.
- (23) Dang, M. T.; Wantz, G.; Bejbouji, H.; Urien, M.; Dautel, O. J.; Vignau, L.; Hirsch, L. Polymeric Solar Cells Based on P3HT:PCBM: Role of the Casting Solvent. Solar Energy Materials and Solar Cells 2011, 95, 3408–3418.
- (24) Kim, D. H.; Park, Y. D.; Jang, Y.; Kim, S.; Cho, K. Solvent Vapor-induced Nanowire Formation in Poly(3-hexylthiophene) Thin Films. *Macromolecular Rapid Communications* **2005**, *26*, 834–839.
- (25) Haid, S.; Marszalek, M.; Mishra, A.; Wielopolski, M.; Teuscher, J.; Moser, J. E.; Humphry-Baker, R.; Zakeeruddin, S. M.; Grätzel, M.; Significant Improvement Bäuerle, Р. of Dye-sensitized Solar Cell Performance by Small Structural Modification in π -conjugated Donor-acceptor Dyes. Advanced Functional Materials 2012, 22, 1291 - 1302.
- (26) Chen, W.; Nikiforov, M. P.; Darling, S. B. Morphology Characterization in Organic

- and Hybrid Solar Cells. *Energy & Environmental Science* **2012**, *5*, 8045–8074.
- (27) Carrillo, J.-M. Y.; Kumar, R.; Goswami, M.; Sumpter, B. G.; Brown, W. M. New Insights into the Dynamics and Morphology of P3HT:PCBM Active Layers in Bulk Heterojunctions. *Physical Chemistry Chemical Physics* **2013**, *15*, 17873.
- (28) Marrink, S. J.; Tieleman, D. P. Perspective on the Martini Model. *Chemical Society reviews* **2013**, 42, 6801–6822.
- (29) Huang, J.; Ie, Y.; Karakawa, M.; Aso, Y. Low Band-gap Donoracceptor Copolymers Based on Dioxocylopenta[c]thiophene Derivatives As Acceptor Units: Synthesis, Properties, and Photovoltaic Performances. J. Mater. Chem. A 2013,
- (30) Miller, E. D.; Jones, M. L.; Jankowski, E. Enhanced Computational Sampling of Perylene and Perylothiophene Packing with Rigid-body Models. *ACS Omega* **2017**, 2, 353–362.
- (31) Liu, S.; Bao, X.; Li, W.; Wu, K.; Xie, G.; Yang, R.; Yang, C. Benzo[1,2- B :4,5- B]dithiophene and Thieno[3,4- C]pyrrole-4,6-dione Based Donor-π-acceptor Conjugated Polymers for High Performance Solar Cells by Rational Structure Modulation. *Macromolecules* **2015**, 48, 2948–2957.
- (32) Beaupré, S.; Shaker-Sepasgozar, S.; Najari, A.; Leclerc, M. Random Da 1 da 2 Terpolymers Based on Benzodithiophene, Thiadiazole[3,4-e]isoindole-5,7-dione and Thieno[3,4-c]pyrrole-4,6-dione for Efficient Polymer Solar Cells. *J. Mater. Chem. A* **2017**, *5*, 6638–6647.
- (33) Jorgensen, W. L.; Tirado-Rives, J. The OPLS [Optimized Potentials for Liquid Simulations] Potential Functions for Proteins, Energy Minimizations for Crystals of Cyclic Peptides and Crambin. *Journal*

- of the American Chemical Society 1988, 110, 1657–1666.
- (34) Martin, M. G.; Siepmann, J. I. Transferable Potentials for Phase Equilibria.
 1. United-atom Description of N-alkanes.
 Journal of Physical Chemistry B 1998,
 102, 2569–2577.
- (35) Yoon, D. Y.; Smith, G. D.; Matsuda, T. A Comparison in Simulations of a United Atom and an Explicit of Polymethylene Atom Model. *The Journal of Chemical Physics* **1993**, *98*, 10037–10043.
- (36) Paul, W.; Yoon, D. Y.; Smith, G. D. An Optimized United Atom Model for Simulations of Polymethylene Melts. *Journal of Chemical Physics* **1995**, *103*, 1702–1709.
- (37) McCoy, J. D.; Curro, J. G. Mapping of Explicit Atom onto United Atom Potentials. *Macromolecules* **1998**, *31*, 9362–9368.
- (38) Tsige, M.; Curro, J. G.; Grest, G. S.; McCoy, J. D. Molecular Dynamics Simulations and Integral Equation Theory of Alkane Chains: Comparison of Explicit and United Atom Models. *Macromolecules* **2003**, *36*, 2158–2164.
- (39) Chen, C.; Depa, P.; Sakai, V. G.; Maranas, J. K.; Lynn, J. W.; Peral, I.; Copley, J. R. D. A Comparison of United Atom, Explicit Atom, and Coarse-grained Simulation Models for Poly(ethylene Oxide). Journal of Chemical Physics 2006, 124, 234901:1–234901:11.
- (40) Nguyen, T. D.; Phillips, C. L.; Anderson, J. a.; Glotzer, S. C. Rigid Body Constraints Realized in Massively-parallel Molecular Dynamics on Graphics Processing Units. Computer Physics Communications 2011, 182, 2307–2313.
- (41) Schwarz, K. N.; Kee, T. W.; Huang, D. M. Coarse-grained Simulations of the Solution-phase Self-assembly of Poly(3-hexylthiophene) Nanostructures. Nanoscale 2013, 5, 2017–2027.

- (42) Shin, H.; Pascal, T. a.; Goddard, W. a.; Kim, H. Scaled Effective Solvent Method for Predicting the Equilibrium Ensemble of Structures with Analysis of Thermodynamic Properties of Amorphous Polyethylene Glycol-water Mixtures. *Journal of Physical Chemistry B* **2013**, *117*, 916–927.
- (43) Anderson, J. A.; Lorenz, C. D.; Travesset, A. General Purpose Molecular Dynamics Simulations Fully Implemented on Graphics Processing Units. *Journal of Computational Physics* **2008**, *227*, 5342–5359.
- (44) Hoover, W. G. Canonical Dynamics: Equilibrium Phase-space Distributions. Physical Review A 1985, 31, 1695–1697.
- (45) Martyna, G. J.; Tobias, D. J.; Klein, M. L. Constant Pressure Molecular Dynamics Algorithms. The Journal of Chemical Physics 1994, 101, 4177–4189.
- (46) Cao, J.; Martyna, G. J. Adiabatic Path Integral Molecular Dynamics Methods. Ii. Algorithms. The Journal of Chemical Physics 1996, 104, 2028–2035.
- (47) Swope, W. C.; Andersen, H. C.; Berens, P. H.; Wilson, K. R. A Computer Simulation Method for the Calculation of Equilibrium Constants for the Formation of Physical Clusters of Molecules: Application to Small Water Clusters. *Journal* of Chemical Physics 1982, 76, 637–649.
- (48) Mateker, W. R.; Heumueller, T.; Cheacharoen, R.; Sachs-Quintana, I. T.; McGehee, M. D.; Warnan, J.; Beaujuge, P. M.; Liu, X.; Bazan, G. C. Molecular Packing and Arrangement Govern the Photo-oxidative Stability of Organic Photovoltaic Materials. Chemistry of Materials 2015, 27, 6345-6353.
- (49) Modestino, M. a.; Chan, E. R.; Hexemer, A.; Urban, J. J.; Segalman, R. a. Controlling Nanorod Self-assembly in Polymer Thin Films. *Macromolecules* 2011, 44, 7364–7371.

- (50) Verploegen, E.; Mondal, R.; Bettinger, C. J.; Sok, S.; Toney, M. F.; Bao, Z. Effects of Thermal Annealing upon the Morphology of Polymer-fullerene Blends. *Advanced Functional Materials* **2010**, *20*, 3519–3529.
- (51) Wunsch, B. H.; Rumi, M.; Tummala, N. R.; Risko, C.; Yen, D.; Steirer, X.; Gantz, J.; Said, M. M.; Armstrong, N. R.; Brédas, J.-L. L. et al. Structureprocessingproperty Correlations in Solution-processed, Small-molecule, Organic Solar Cells. Journal of Materials Chemistry C 2013, 1, 5250.
- (52) Lucas, J. M.; Labastide, J. a.; Wei, L.; Tinkham, J. S.; Barnes, M. D.; Lahti, P. M. Carpenter's Rule Folding in Rigidflexible Block Copolymers with Conjugation-interrupting, Flexible Tethers between Oligophenylenevinylenes. The Journal of Physical Chemistry A 2015, 150630131149000.
- (53) Hunter, J. D. Matplotlib: A 2d Graphics Environment. Computing In Science & Engineering 2007, 9, 90–95.
- (54) Zhai, L.; Khondaker, S. I.; Thomas, J.; Shen, C.; McInnis, M. Ordered Conjugated Polymer Nano- and Microstructures: Structure Control for Improved Performance of Organic Electronics. Nano Today 2014, 9, 705–721.
- (55) Sato, M.; Kumada, A.; Hidaka, K.; Hirano, T.; Sato, F. Quantum Chemical Calculation of Hole Transport Properties in Crystalline Polyethylene. *IEEE Transactions on Dielectrics and Electrical Insulation* 2016, 23, 3045–3052.
- (56) Humphrey, W.; Dalke, A.; Schulten, K. VMD: Visual Molecular Dynamics. Journal of Molecular Graphics 1996, 14, 33– 38.
- (57) VMD Web Page. http://www.ks.uiuc.edu/Research/vmd/, Accessed: 2017-11-02.

- (58) Rakhmanov, E. A.; Saff, E. B.; Zhou, Y. M. Minimal Discrete Energy on the Sphere. *Mathematical Research Letters* **1994**, *1*, 647–662.
- (59) Hauptman, H. The Phase Problem of X-ray Crystallography. 1983.
- (60) Zou, Y.; Najari, A.; Berrouard, P.; Beaupre, S.; Aïch, B. R.; Tao, Y.; Leclerc, M. A Thieno[3, 4-c]pyrrole-4, 6-dione-based Copolymer for Efficient Solar Cells. *Journal of the American Chemical Society* **2010**, *132*, 5330–5331.
- (61) Braunecker, W. A.; Owczarczyk, Z. R.; Garcia, A.; Kopidakis, N.; Larsen, R. E.; Hammond, S. R.; Ginley, D. S.; Olson, D. C. Benzodithiophene and Imidebased Copolymers for Photovoltaic Applications. *Chemistry of Materials* **2012**, *24*, 1346–1356.
- (62) Lin, Y.-H.; Yager, K. G.; Stewart, B.; Verduzco, R. Lamellar and Liquid Crystal Ordering in Solvent-annealed All-conjugated Block Copolymers. Soft Matter 2014, 10, 3817–3825.
- (63) Towns, J.; Cockerill, T.; Dahan, M.; Foster, I.; Gaither, K.; Grimshaw, A.; Hazlewood, V.; Lathrop, S.; Lifka, D.; Peterson, G. D. et al. XSEDE: Accelerating Scientific Discovery. *Computing in Science & Engineering* **2014**, *16*, 62–74.

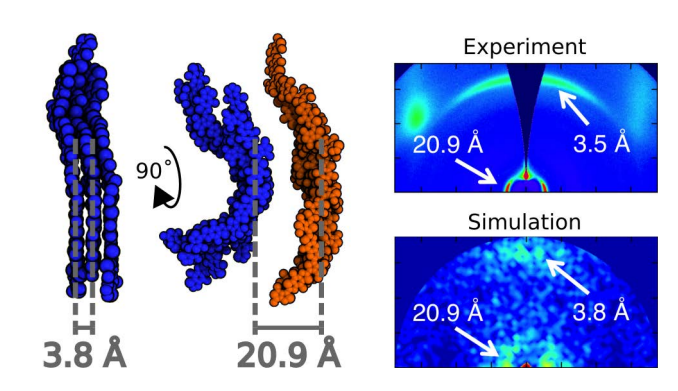


Figure 12: For Table of Contents Only